Materials Advances

ROYAL SOCIETY OF CHEMISTRY

PAPER

View Article Online
View Journal | View Issue

Cite this: *Mater. Adv.*, 2025, **6**, 6894

Revolutionizing environmental clean-up: novel CORN-MOF-2/PVDF composite membranes for the removal of multi-pollutants

Usha Nellur and Mahesh Padaki *

The increasing prevalence of complex multi-pollutants, including heavy metals, dyes, and pharmaceutical residues, in wastewater streams demands advanced materials capable of efficient and selective separation. This study addresses the critical challenge of removal of diverse pollutants by developing CORN-MOF-2/PVDF composite membranes, in which novel CORN-MOF-2(Ce) was functionalized into a PVDF matrix by a nonsolvent-induced phase-inversion method (NIPS). The introduced MOF enhanced the hydrophilicity of the resulting membranes and provided a higher permeability of 434.95 L m^{-2} h^{-1} bar^{-1}. Membrane performance was evaluated through a series of filtration tests using synthetic wastewater containing heavy metal ions, dyes and pharmaceutical compounds. The CORN-MOF-2/PVDF membranes transitioned into a more selective interface, leading to absolute rejection of a wide range of pollutants—99% for dopamine hydrochloride (DP), $Cr_2O_7^{2-}$, Alcian blue (AB), and Congo red (CR). Furthermore, the study extended to investigate the removal efficiency of the optimized membrane under different pH conditions, achieving optimal performance at neutral pH. A combination of size exclusion, affinity-based bonding, and charge-based interactions was followed to attain superior rejection rates. The simultaneous removal of multiple pollutants from the aqueous system demonstrates the superior versatility and efficiency of the fabricated membranes in handling complex multi-component contaminations. The treated water resulting from this work adheres to the WHO's standards for safe water. Additionally, antifouling studies showed a flux recovery ratio of >95% after multiple cycles.

Received 3rd June 2025,
Accepted 11th August 2025

DOI: 10.1039/d5ma00581g

rsc.li/materials-advances

1. Introduction

The tannery sector contributes significantly to the economy. About 80% of the leather produced worldwide is made by mineral tanning, also known as chrome tanning, which is the most popular process for turning animal skin into leather.[1,2] The extensive use of chemicals and water results in highly polluted wastewater, posing a serious environmental risk. Tannery effluent contains high concentrations of Cr/Cr(III)/Cr(VI), organic pollutants (acidic and anionic dyes), and other inorganic constituents.[3,4] This complex waste, when disposed of in a wastewater treatment plant, combined with pharmaceutically active compounds (PhACs) from the household wastewater (sewage) becomes even more complex to remove all the harmful contaminants. PhACs are substances that include antibiotics, antipyretics, anti-inflammatories, and analgesics and are frequently found in wastewater effluents at various concentrations of ppt (ng L^{-1}) or even ppm (mg L^{-1}) levels.[5] Unmetabolized forms of PhACs are released into the aquatic environment *via* human and animal faeces and urine, as well as by wastewater from medical facilities and pharmaceutical manufacturing facilities. Together, these various sources lead to the PhAC contamination of water bodies. Adsorption is well-explored in removing aquatic pollutants; however, secondary pollution results from the regeneration of the adsorbent and the disposal of the desorption solution.[6,7] Catalytic degradation can produce toxic disinfection by-products, worsening the situation and consuming relatively high energy.[8] In this context, membrane separation is a promising solution in terms of productivity and reusability. Nanofiltration (NF) membranes exhibit good separation performance in rejecting nearly all pollutants with particle sizes larger than the pore size (0.5–2 nm).[9]

Metal–organic frameworks (MOFs) have gained considerable attention as nanofillers in membranes owing to their exceptional properties, including large surface area, tunable pore sizes, and versatile chemical functionalities. According to the literature, pore-networked membranes PNM/PEBA incorporated with metal–organic polyhedra simultaneously worked in the removal and detection of OCR, EHMC, and HMS, offering high selectivity and adsorption capacity.[10] Free-standing

Centre for Nano and Material Sciences, Jain University, Jain Global Campus, Kanakapura, Ramanagaram, Bangalore 562112, India.
E-mail: sp.mahesh@jainuniversity.ac.in; Tel: +919538414994

polyacrylonitrile/MOF-808 mixed-matrix membranes effectively removed 91% of DCF from the water. The advent of a large surface area of the MOF and the surface charge of DCF improved the adsorptive removal of DCF.[11] A TFN-CU5 membrane incorporated with C-UiO-66-NH_2 had a high water permeance of 17.66 L m^{-2} h^{-1} bar^{-1}, exceptional rejection for norfloxacin (97.92%) and ofloxacin (95.31%), and excellent long-term stability for treating synthetic secondary effluents with an antibiotic rejection rate of over 90%.[12] MOF materials hold great potential for the separation and filtration of pharmaceutical actives because of their distinct structural features.[13] However, some potential downsides and restrictions can impact their effectiveness and practicality in removing multiple pollutants from complex sewage wastewater. Membrane technologies are often limited to targeting specific classes of pollutants, such as dyes, heavy metals, or pharmaceutical compounds, necessitating separate treatment processes for each type of contaminant. This approach increases the operational complexity and also elevates treatment costs and energy consumption. A potential membrane capable of simultaneously targeting multiple pollutants, *i.e.* removing dyes, heavy metals, and pharmaceutical compounds in a single treatment step, is highly necessary to treat sewage wastewater.

Generally, aromatic bicarboxylic acids are chosen as organic linkers for MOF synthesis. Most of these are synthetic and, hence, expensive. To replace these, natural dicarboxylate compounds extracted from biomass are desirable. In light of this, we chose itaconic acid extracted from *Aspergillus itaconicus* and *Aspergillus terreus* fungi *via* fermentation as a sustainable raw material (organic linker). Cerium, a typical nuclide, recovered from radioactive waste is used to synthesize a novel cerium-based MOF (CORN-MOF-2).[14,15] However, Zr-based CORN-MOF-2 has been reported earlier by Chen and group and studied for gas storage.[16] According to the literature, the Ce-MOFs are well known for their great potential for the removal of multipollutants (heavy metals, dyes, pharmaceuticals, and nuclear waste).[17–21] Ce^{4+}, with partially filled low-lying 4f orbitals, readily forms complexes with organic compounds. However, CORN-MOF-2(Ce) has not been reported yet in water purification. In general, MOFs are prepared *via* solvothermal routes employing high-temperature and -pressure conditions, leading to higher energy consumption and lesser product yield. Furthermore, reported CORN-MOF-2(Zr) is desirable for a certain class of pollutants. Herein, we report CORN-MOF-2(Ce) for the first time, with a set of additional features such as simple room-temperature synthesis within 30 minutes using water as a solvent. Further, incorporating the as-synthesized MOF into the PVDF matrix resulted in composite membranes. The unique structural and chemical properties of MOFs, including tunable pore size, and carboxylate and Ce^{4+} functionalities, allow modified membranes to efficiently capture and remove multiple pollutant types. We investigated the removal efficiency of heavy metals, namely $Cr_2O_7^{2-}$, dyes, namely Congo red (CR) and Alcian blue (AB), PhACs, namely dopamine (DP), diclofenac sodium (DCF), and naproxen (NP), and revealed that synergistic mechanisms such as adsorption, size exclusion, and chemical (non-covalent) interactions are underplayed. This multifunctionality of PVDF/MOF-2 composite membranes offers significant advantages over traditional membranes. The membrane systems reported to date are typically optimized for the removal of individual pollutants, often requiring extensive modification or the integration of multiple treatment units to achieve comparable results. The novelty of reported membranes lies in their ability to address the challenges of mixed pollutant scenarios with better efficiency and versatility. The treatment of diverse contaminants by a single membrane enhances operational simplicity and contributes to the development of sustainable and cost-effective water purification technologies.

2. Results and discussion

2.1 Characterization of CORN-MOF-2(Ce)

The observed lowest angle reflection at $2\theta = 8.7^\circ$ corresponding to the (111) plane in the PXRD pattern of the MOF depicts the semi-crystalline nature of the framework (Fig. 1(a)), consistent with the previous reports.[16,22] It was experimented that the replacement of solvent–water with DMF resulted in an amorphous framework. In the presence of a base (DMF), complete desolvation of precursors led to amorphization of the product. However, synthesis under aqueous conditions regulated desolvation giving semi-crystallites. The FT-IR spectrum of the MOF was studied in the 4000–400 cm^{-1} region. Fig. 1(b) presents the bands in the 1690–1630 cm^{-1} region corresponding to the symmetric and asymmetric ν_{COOH} stretching vibrations in the itaconic acid linker, which shifted to 1510 cm^{-1} ν_{COO^-} in the case of CORN-MOF-2. This manifests the deprotonation of –COOH groups and the co-ordination of itaconate to Ce^{4+}. Further, the $\nu_{C=O}$ stretching band at 1224 cm^{-1} in itaconic acid shifted to 1195 cm^{-1} in the MOF due to the co-ordination.[23,24] ν_{sym} and ν_{asym} bands of $-CH_2$ and $-CH_3$ appeared at 2940 and 2746 cm^{-1}. The bands related to the bending vibrations of the C–O group in the lower wavenumber region of 700–640 cm^{-1} are also observed in itaconic acid and the MOF. These observations conclude that linker carboxylic functionalities are co-ordinated to the Ce^{4+} nodes, forming the corn-like framework.

XPS analyzed the C 1s, O 1s, and Ce 3d spectra of the MOF and their relative amounts in the survey spectra (Fig. S1a). Deconvoluted peaks at 885.21, 907.07, 882.15, 899.96, 903.24, and 916.65 eV confirm the presence of cerium in both the oxidation states (IV) and (III) in the framework corresponding to the $3d_{5/2}$ and $3d_{3/2}$ states, respectively (Fig. 1(e)).[25,26] Two different peaks can distinguish between carbon atoms in various chemical environments, such as 284.85 eV for C–C bonds in the fumarate linker, 288.41 eV for C=O bonds in the carboxylate groups, and any potential C–O bonds from surface-adsorbed species (Fig. 1(c)). Oxygen in the Ce–O bonds of the cerium oxide secondary binding units (SBUs) is designated by 531.32 eV and C=O bonds of the linker by peak centered at 531.79 eV (Fig. 1(d)). N_2 sorption studies revealed the BET-specific surface area (SSA) of 231.42 m^2 g^{-1} (Fig. 1(f)),

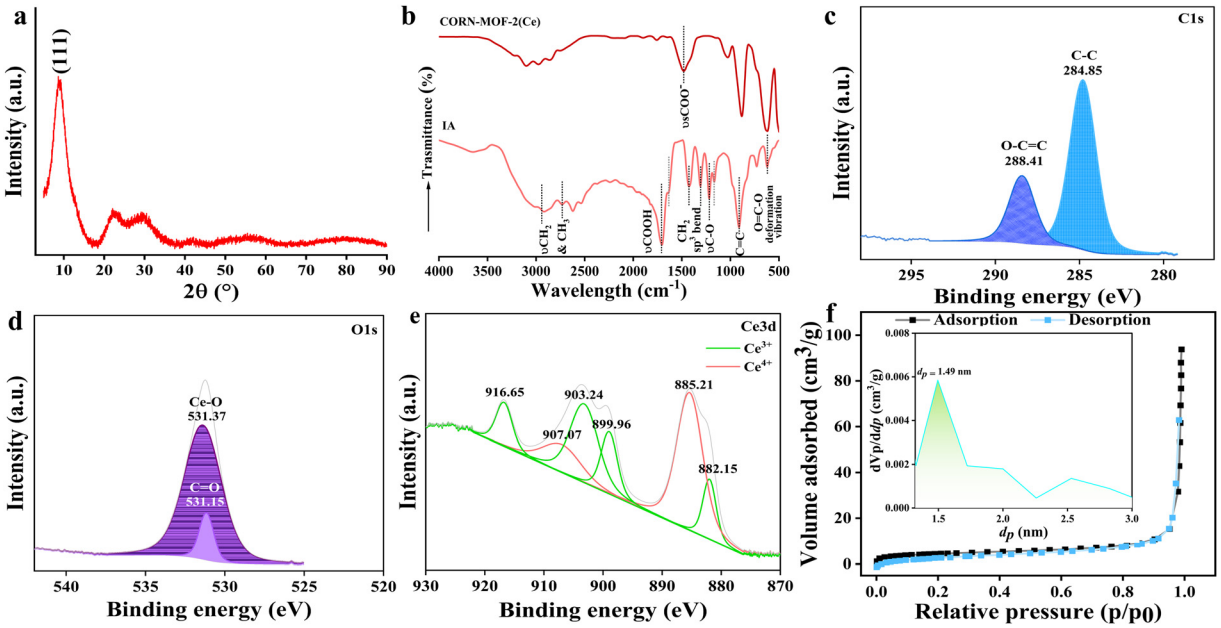

Fig. 1 Structural characteristics of the MOF: (a) PXRD pattern; (b) FT-IR spectra; XPS spectrum of (c) C 1s, (d) O 1s, and (e) Ce 3d; (f) BET N_2-sorption isotherm and BJH plot (inset).

and pore size distribution analysis disclosed micropores approximately 1.49 nm in diameter (Fig. 1(f) inset).

The MOF resembled a corn shape as shown in Fig. 2(a) and (b). The acquired FESEM and TEM images are presented in Fig. 2(c)–(e). A spherical morphology of CORN-MOF-2 was identified. Further, TEM was employed to analyze the structural characteristics, crystallinity, and morphology. The TEM images showcased the spherical structural arrangement with an average grain size of 61–64 nm (Fig. 2(d) and (e)). Diffused diffraction rings or halos in the SAED pattern indicated the presence of semi-ordered regions that are characteristic of the semi-crystalline MOF (Fig. 2(f)). Discrete spots superimposed on the diffuse rings represented the crystalline domains within the material. The spots are less sharp and fewer in number compared to a fully crystalline MOF, reflecting the limited size or distribution of the crystalline regions in agreement with the PXRD pattern. The EDX mapping gives the elemental composition (carbon: 24.17%; oxygen: 31.24%; cerium: 44.59%), as shown Fig. S1b.

2.2 Characterization of MOF membranes

2.2.1 Intrinsic properties. The effects of MOF materials and various changes in the membrane structure are examined by XRD analysis. The XRD patterns of unmodified and modified PVDF membranes are presented in Fig. 3(a). The α(010) and α(100) planes characteristic of the α-phase (♦) PVDF were reflected at $2\theta = 18.3^\circ$ and 21° in all four membranes.[27,28] The appearance of a peak at 28.3° for the modified membranes indicated the influence of CORN-MOF-2 on polymer phases with increasing intensity related to the increasing concentration of MOF. The polymer crystallization behavior was influenced by the MOF, as it acts as a nucleating agent, thereby

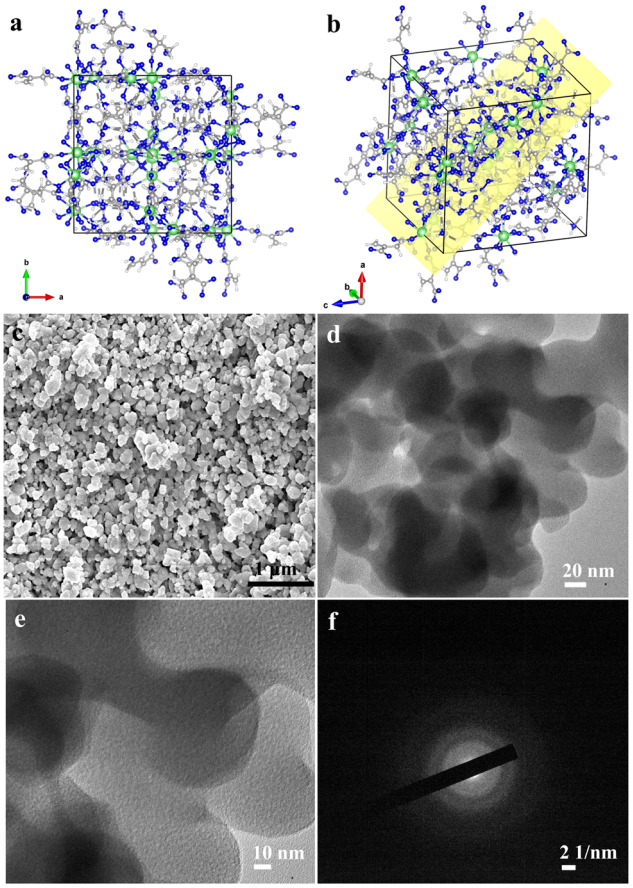

Fig. 2 (a) and (b) Architectures of CORN-MOF-2(Ce), (c) FESEM, (d) and (e) HRTEM images, and (f) SAED pattern of CORN-MOF-2(Ce).

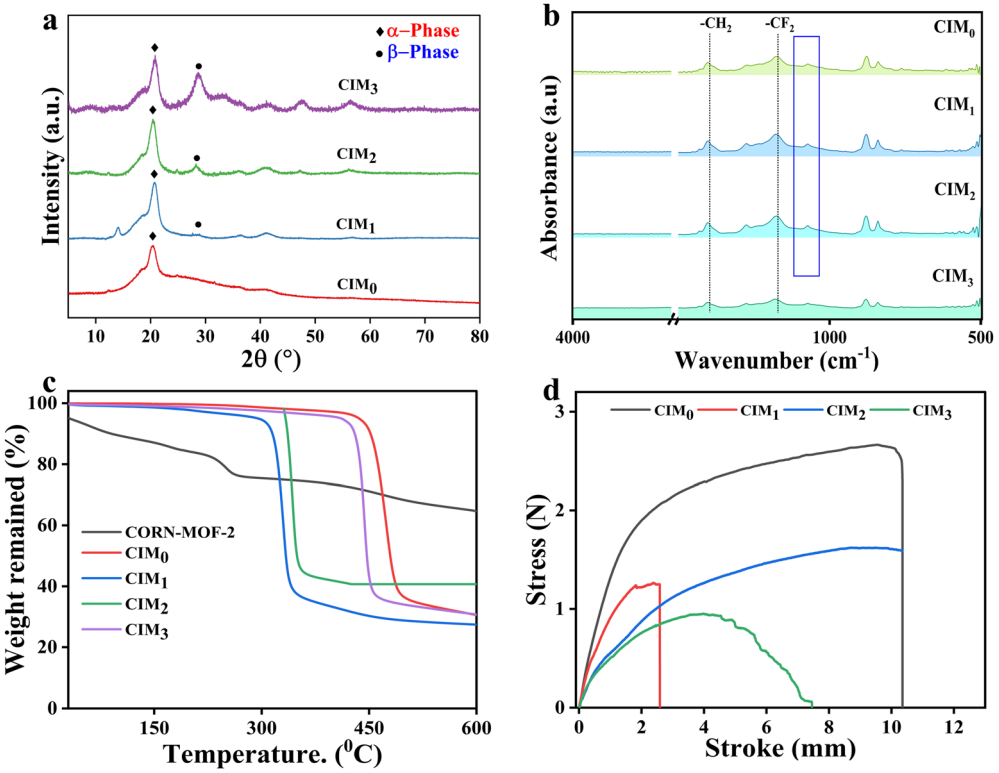

Fig. 3 (a) XRD pattern, (b) ATR-IR spectra, (c) TGA curves, and (d) Stress–stroke curves of modified PVDF membranes.

preferring the PVDF to align in the β-phase (●) partially along with the α-phase.[29] The β-phase has a more rigid chain alignment compared to α, which further enhances the mechanical strength and structural stability of the membrane. The van der Waals (Ce^{4+}–F^{-}) interactions imposed this polymer transition, thus explicitly imprinting the reflection of the MOF in the XRD profile of the modified membranes.

By ATR-IR spectroscopy, the PVDF/MOF membranes were scrutinized for functional group characterization. Comparing the pristine and modified PVDF membranes, the appearance of a peak at 1278 cm^{-1} signaled the β-phase of PVDF in the modified membranes (Fig. 3(b)). This supported the *trans*-conformation of the PVDF chain in modified membranes as inferred from XRD.[29] The stretching and deformation vibrations of $–CH_2$ and $–CF_2$ groups appeared at 1400 and 1172 cm^{-1}, respectively, for all the four membranes.[30] Bands at 879 and 1070 cm^{-1} were skeletal C–C stretching vibrations, and that at 842 cm^{-1} was assigned to the $–CH_2$ in-plane rocking vibration. The ATR-IR spectra of the MOF-membranes showed no new bands because the interactions between PVDF and the MOF were non-covalent (van der Waals forces; Fig. 8). Nevertheless, the phase change developed as a clear confirmation that MOF had been inserted into the polymeric domain.

The thermogravimetric analysis of the MOF and membranes is shown in Fig. 3(c). CORN-MOF-2 has decomposed in two stages. The first weight loss (∼20%) started at 30 °C and continued up to 260 °C, including the loss of adsorbed moisture and solvent molecules/atmospheric gas trapped within the pores during the synthesis of the MOF. The second gradual weight loss (∼7%) up to 450 °C is attributed to the disintegration of linkers and denaturation of the framework.[31] The as-synthesized MOF was thermally stable up to 450 °C. Comparing the thermal stability of modified membranes with the MOF, weight loss events of membranes were predominated by the parent PVDF. Since there were only non-covalent interactions between PVDF and the MOF, as confirmed by ATR-IR spectroscopy, and no other physical bonding interactions were involved. Three weight losses were noticed for the membranes. The first loss up (∼1%) to 100 °C corresponded to the escape of physically adsorbed moisture. The second steep weight loss (∼62%) was seen in the range of 100–430 °C, indicating the breakdown of the C–F and C–C bonds. The last weight loss of ∼10% beyond 500 °C is related to the complete dismantling of the PVDF polymeric backbone.[32,33] The thermograms of the modified membranes leaned towards the parent PVDF in the order of CIM_3- CIM_2-CIM_1, corresponding to the increasing MOF concentrations of 5, 6, and 7 wt%. This further substantiated the variation in the MOF concentration in the modified membranes.

In wastewater treatment, the membranes are expected to be strong enough to withstand the pressure and function for a long time. Insufficient mechanical strength can cause the membrane to deform and rupture during filtration. Tensile testing was used in this study to examine the mechanical properties of the fabricated membranes. Fig. 3(d) displays the stress–strain curves and tensile strength of the MOF membranes. A membrane with a higher elongation at break is more

Table 1 Physico-chemical properties of the modified PVDF membranes

Membrane	Thickness (μm)	Tensile strength (MPa)	Elongation at break (%)	Porosity (%)	Water uptake (%)	Contact angle (°)
CIM_0	37.90 ± 0.89	0.328	25.95	71.35 ± 0.26	58.94 ± 0.89	73.83 ± 0.97
CIM_1	49.02 ± 1.5	0.155	6.37	89.46 ± 1.09	78.97 ± 1.5	66.75 ± 1.45
CIM_2	56.7 ± 1.82	0.198	25.86	92.11 ± 0.46	86.08 ± 1.82	60.30 ± 0.13
CIM_3	63.2 ± 0.91	0.008	18.65	93.99 ± 1.34	91.01 ± 0.91	59.45 ± 0.15

flexible and ductile. This means that the membrane can undergo more deformation before breaking. A membrane with a higher tensile strength can withstand greater tension without rupturing.[34] For the pristine PVDF membrane, the tensile strength was 0.32 MPa and elongation at break was 25.95% (Table 1).[35,36] After the MOF is inserted into the PVDF matrix, the tensile strength and elongation at break are decreased initially and then increased. In the case of initial MOF loading (5 wt%), the MOF particles disrupt the structural continuity of the polymer chains.

This reduces the mechanical integrity of the membrane (0.15 MPa) because the cohesive forces within the matrix are compromised. In the case of CIM_2 (6 wt% of MOF), uniform dispersion and higher surface area of the MOF establish more interfacial interactions with the polymer. Moreover, the increasing porosity (Table 1) allows applied stress to be distributed more evenly throughout the membrane. This combined effect increases the tensile strength to 0.19 MPa. Beyond 6 wt%, the molecular force between the MOF particles increases, whereas the molecular force between the MOF particles and the polymer decreases, causing the MOF particles to aggregate. It also makes the membrane more rigid, which reduces its mechanical stability.[37] The extremely porous structure of the CIM_3 membrane creates voids, which, in turn, act as weak points to withstand tensile forces. The tensile strength is positively impacted by the optimal amount of the MOF, while the mechanical strength is weakened by excessive amounts of the MOF. Therefore, 6 wt% is the optimal MOF loading with a tensile strength of 0.19 MPa.

2.2.2 Intrinsic properties. The morphology of pristine and composite membranes was investigated through the top and cross-sectional FESEM images. EDX mapping on the CIM_3 membrane surface gives the elemental composition: carbon, 35%; oxygen, 25%; fluorine, 31%; and cerium, 6% (Fig. S2e). The top surface images appeared to be well dispersed without surface nanoparticle agglomeration (Fig. S2a–d). The cross-sectional SEM images revealed an asymmetric membrane structure with a dense thin top layer, a middle layer with porous channels, and a thick bottom layer. The parent PVDF membrane showed sparse short channel-like structures (Fig. 4(a) and (d)). Incorporating CORN-MOF-2 increased the porosity of the membrane. Wider and longer channels were observed in the case of CIM_1, and this increase in the porous bulk of the middle layer reduced the thickness of the bottom layer.[38] This seemed to continue as the MOF loading increased. However, the overall thickness of the membrane increased as the MOF concentration increased. The thickness of these membranes increased up to two times upon adding the MOF. The viscosity of the dope solution following the addition of MOF increased. A thicker membrane will result from a highly viscous dope solution compared to a less viscous bare dope solution.[39] The addition of the hydrophilic MOF induces the diffusion rates of the solvent–nonsolvent during the phase inversion process. The faster the diffusion, the longer the porous channels. A gradual increase in MOF content extended the effect of enhanced diffusion, resulting in highly porous structures.[40,41] These morphological modifications improved the permeability of the modified membranes.

In addition to the changes in the membrane morphology, the surface roughness was measured using AFM. Added MOF particles brought significant changes in the surface topography of the membranes. As shown in Fig. 4(e)–(h), the parent PVDF membrane has a surface roughness of 13.52 ± 42 nm. A consistent increase in the surface roughness of composite membranes, 17.73 ± 0.82, 19.20 ± 0.57, and 20.58 ± 0.37 nm corresponding to CIM_1, CIM_2, and CIM_3, indicated a significantly rougher surface. The tendency of hydrophilic MOF particles to emerge to the membrane surface during the NIPS produces ridges and valleys. These ridges and valleys created the visual folds with a fluctuating surface noticed in contrast to that of the unmodified membrane. The observations were evident from the FESEM top images. The changes in surface roughness further altered the surface hydrophilicity of the membrane. The higher the MOF concentration, the rougher the membrane surface observed. The rougher the surface, the higher the surface area of contact with the target pollutants.[42] Thus, the modified membranes with rougher surfaces will have elevated rejection rates for the target pollutants.

2.2.3 Membrane surface hydrophilicity and charge. The membrane hydrophilicity was evaluated through water uptake, porosity, and water contact angle data. Table 1 presents the water uptake (WU) and contact angle (CA) values. As discussed earlier, the surface roughness of the membrane directly affects the membrane hydrophilicity. This can be substantiated by the CA values. Since the parent PVDF has a comparatively smoother surface, a higher CA value of 73.83° was noted.[43] For the modified membranes, as the surface roughness increased proportionately, the CA values were decreased. A lower CA suggests a higher surface hydrophilicity. A 7 wt% membrane with a CA value of 59.45° indicated a highly hydrophilic surface compared to the other two membranes, namely, CIM_1 and CIM_2 with CA values of −66.75° and 60.30°, respectively. The results established that the presence of hydrophilic $–COO^-$ groups of the MOF introduced into the PVDF matrix enhanced the tendency of the membrane surface to wet easily. When the MOF loading increased, more number of $–COO^-$ groups were

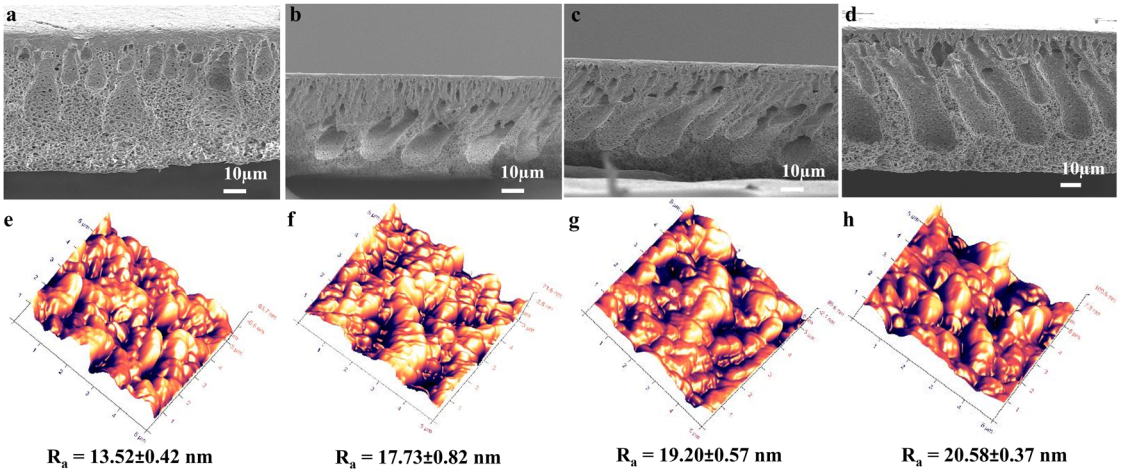

Fig. 4 Morphological and topological features: (a)–(d). FESEM cross-sectional images and (e)–(h). AFM images of the modified PVDF membranes.

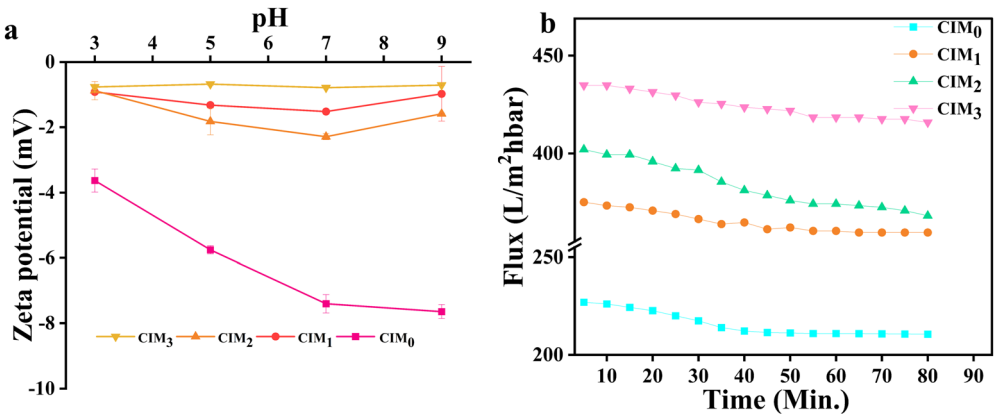

Fig. 5 (a) Surface charge and (b) pure water permeability of the MOF membranes.

present, resulting in more hydrophilicity with a lower CA value. Similarly, the hydrophilic moieties of the MOF induce the formation of porous structures, as discussed from the cross-section FESEM images. The porous channels facilitate easy movement of water through the membrane, increasing the water uptake. The MOF concentration has a linear influence on the porosity of membranes. Increasing the MOF content increased the overall porosity of the membrane, in turn, increasing the water uptake. A porosity of 71.35% was noticed for the CIM_0 membrane, whereas loading 5 wt% MOF resulted in 18% hike in porosity, implying that 89.46% was recorded for CIM_1.[44] Further, 6 wt% and 7 wt% MOF loadings led to an increase in porosity to 92.11% and 93.99% for CIM_2 and CIM_3, respectively. Together with porosity, the water uptake of these membranes reached 78.97%, 86.08% and 91.01% for CIM_1, CIM_2 and CIM_3, respectively, much higher than that of the parent PVDF membrane (WU-58.94%). These results proved a strong positive linear correlation between the porosity and water uptake of the membranes. This modification assisted in increasing the permeation flux.[45]

The surface charge characteristics of the membranes at different pH values (3, 5, 7 and 9) were measured using a zeta potential instrument. Fig. 5(a) shows the zeta values of all the membranes. The surface charge of the plain PVDF membrane was −7.40 mV in neutral pH. As the pH turned acidic (pH-3 and 5), the negative charge of the plain PVDF membrane decreased to −3.62 and −5.75 mV, respectively. This is due to the complete protonation of the negatively charged $-COO^-$ groups in acidic pH values. In the case of basic conditions, pH 9, the deprotonation of –COOH groups decreased the surface charge to −7.71 mV.[46] The same trend was shown in MOF-infused membranes. CIM_1 exhibited a surface charge of −1.51 mV at neutral pH values, reduced to −0.87 mV at acidic pH values, and slightly increased to −0.97 mV at pH 9. For CIM_2, a slightly higher concentration of MOF (6 wt%) could add to the negative charge of the PVDF, giving a −2.29 mV charge at pH 7. However, the further increased MOF content (7 wt%) nullified all the charge effects and reached an almost near-zero (−0.57 mV) surface charge. The change in pH did not alter the surface charge in the case of CIM_3. The measured surface charge of CORN-MOF-2 in neutral pH was −1.46 mV. The addition of negatively charged MOFs was expected to increase the negative charge of membranes. However, this was the contrary. Because the integration of MOF results in a molecular

structure change in the PVDF matrix such as altering functional group exposure. From the XRD patterns, details on the phase transition from α to β were obtained. The β-phase alignment involves all the fluoride atoms on one side and hydrogen atoms on the other side. The possibility is that the PVDF matrix might expose fluoride atoms facing down (rear to the surface) and hydrogen atoms facing up (near the surface) during the fabrication process, counteracting the influence of the negatively charged MOF. Therefore, the optimal loading of 6 wt% MOF influenced the maximum negative charge, achieving a surface charge of −2.29 mV.

2.3 Membrane performance

2.3.1 Pure water permeation. A thorough assessment of the physiochemical characteristics of membranes provided an understanding of the pure water permeation profile of composite membranes. An optimization process covered different pressure conditions (1–6 bar) to attain a stable enhanced water flux. Membranes reached a stabilized constant flux at a pressure of 4 bar. However, beyond 4 bar, the permeability increased but was not constant over a reasonable time. In Fig. 5(b), the permeability of the modified membranes showed a growing trend, attaining a two-fold enhancement for CIM_3 (434.95 ± 11.72 L m^{-2} h^{-1} bar^{-1}) when compared to the parent PVDF membrane (227.00 ± 12.27 L m^{-2} h^{-1} bar^{-1}). This means that the permeability increased as the MOF concentration increased. The combined advent of increasing porosity and water uptake enhanced the hydrophilicity of the membrane. The variations in membrane thickness also impacted the permeation. Increasing membrane thickness generally decreases the membrane permeability, as the distance feed molecules travel to pass through the membrane increases in a considered time frame.[47] From CIM_0 to CIM_3, membranes are much thicker than the parent PVDF membrane (Table 1). Interestingly, the membrane permeability has increased rather than decreased. A close inspection of porous channels from the cross-section (Fig. 4(a)–(d)) revealed that the nanochannels of membranes are growing relatively long, reaching the bottom layer, and wider too. This implies that the opening of these channels is wider than that of the PVDF membrane. Therefore, the molecule passing through the narrower channel (pristine PVDF) feels more strained than that in the case of wider channels ($CIM_1 < CIM_2 < CIM_3$) even though the distance is longer. Thus, the active transport mechanism is less affected by thickness compared to the pore diameter. An extremely thick membrane could still speed the water transport regardless of the structural constraints. Given the pure water permeation profile, further purification studies were carried out to investigate the efficiency of membranes. Given the specified pure water permeation profile, further purification studies were carried out for the membranes at a pressure of 4 bar, with an emphasis on membranes that functioned at low pressures but presented improved flux.

2.3.2 Removal studies. At first, PVDF/CORN-MOF-2 membranes were tested for the removal of PhACs. Three different pharmaceutically active compounds, namely, DP (+), DCF (−), and NP (neutral/partially negative) were chosen. The flux and rejection profiles are presented in Fig. 6(a)–(c). It is noticed that the flux in all three PhACs increased as the pressure increased along with the increase in MOF content alike pure water flux. The values presented in Fig. 6(a)–(c) indicate no rejection for DP and NP and a poor rejection of 25% for DCF with minimal fluxes of 10.72, 21.28, and 10.71 L m^{-2} h^{-1}, respectively, in the case of the pristine PVDF membrane. Fig. 6(b) shows that

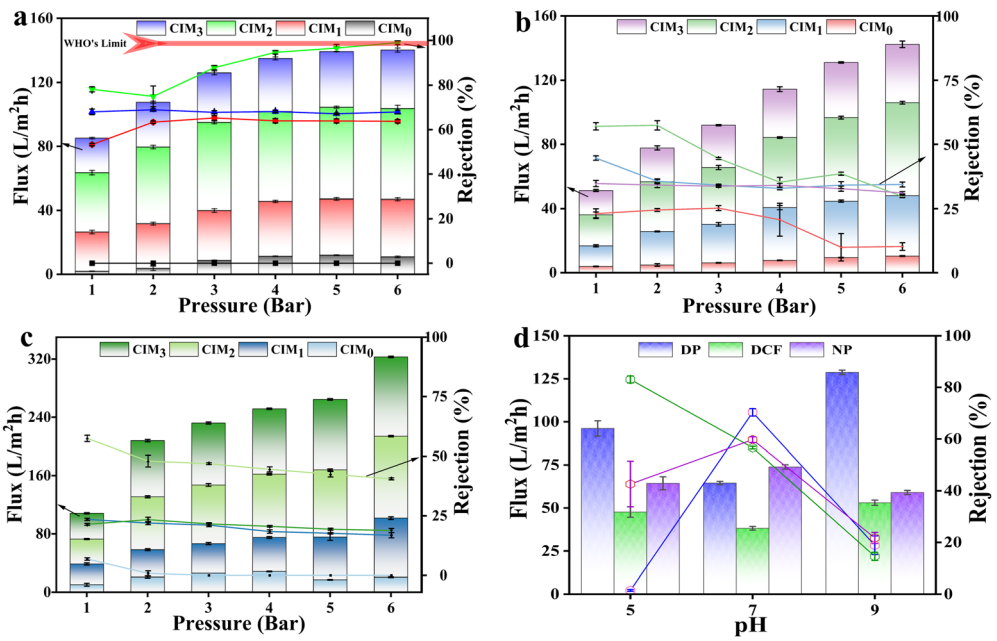

Fig. 6 Flux-rejection graphs of (a) DP, (b) DCF, and (c) NP for MOF-membranes. (d) Effect of pH on the rejection trend (for the optimized CIM_2 membrane).

PhAC-flux for CIM_1 ranged between 26 and 41 L m^{-2} h^{-1} with a rejection rate of ~32% for DCF, 23–40 L m^{-2} h^{-1} with a rejection of ~63% for DP (Fig. 6(a)), and 38–77 L m^{-2} h^{-1} with a poor rejection of ~20% NP at a pressure of 1–6 bars (Fig. 6(c)). PhAC-flux for CIM_2 and CIM_3 further increased reaching 140 L m^{-2} h^{-1}, and the rejection efficiency reached an optimum stage of ~99%, ~54%, and ~58% for CIM_2 during DP, DCF, and NP filtrations, respectively. Over changing the pressure scale, CIM_2 upheld the rejection to be uniform. For CIM_3, the rejection efficiency decreased as expected due to the presence of larger pores in the membrane channels. Overall, it is noteworthy that the increasing MOF content significantly influenced the enhanced rejection trend compared to the plain PVDF membrane.

Considering the mechanism behind the observed rejection rates, DP, positively charged in its hydrochloride form, causes strong attractive electrostatic interactions with the negatively charged membrane surface boosting the rejection. DCF, negatively charged drug, is expected to be rejected by electrostatic repulsion however, experiences partial rejection of ~54% due to hydrophobicity interactions. At neutral pH values, NP is less ionized or may be neutral/slightly negatively charged. The lower electrostatic repulsion with the negatively charged membrane surface allows it to pass more freely, thus giving a poor rejection irrespective of the membrane with a higher MOF content. However, the rejection profile remained comparable in the range of 50–55% for DCF and NP. This was mostly attributed to the minor adsorption and size-exclusion principle that governs the membrane filtrations.[48,49]

Moving forward, the removal efficiency of membranes was analyzed at different pH values to understand the impact of the pH. Given the best rejection profile with decent flux, CIM_2 was screened for further filtration studies. The removal studies of DP, DCF, and NP at pH 5, 7 and 9 at a constant pressure of 4 bar are presented in Fig. 6(d). The peak performance was observed at neutral pH, the same as designated above. This can be explained as the interplay between the ionization state, membrane surface charge, and the electrostatic interactions. Pointing to the structures of PhACs, they have functional groups such as –OH, –COOH, and –NH_2 (–NRH, R-alkyl), which undergo ionization/deionization, depending on the pH considered. At acidic pH 5, the specified functional groups will be protonated imparting an overall positive charge, thereby experiencing a weak electrostatic attraction with a slightly negatively charged (−1.82 mV) CIM_2 surface. The same scenario is observed at pH 9. The highest negative charge of −2.29 mV has set the optimal electrostatic attraction between PhACs and CIM_2 at pH 7. This accomplished a peak rejection at pH 7 except DCF. DCF having both –COO^- and –NRH groups is a weakly acidic compound with a pK_a value of ~4.0. At pH 5, DCF is partially ionized existing in both protonated (neutral) and deprotonated (negatively charged) forms. Neutral DCF molecules are less likely to pass through the membrane due to other rejection mechanisms such as size exclusion and hydrophobic interactions. Thus, rejection is maximum at pH 5. At pH 7 and 9, DCF is fully deprotonated, existing almost entirely in its negatively charged form, which is highly water soluble and less likely to adsorb onto the membrane surface. This reduces interactions with the membrane and increases the permeability. Thus, poor rejection is observed at pH 7 and 9.

Furthermore, a heavy metal ($Cr_2O_7^{2-}$) removal study was conducted to assess the membrane efficiency. The flux-rejection behaviour of MOF-membranes is displayed in Fig. 7(a). The flux was found increasing from 24.21 ± 0.22 to 59.25 ± 0.48 L m^{-2} h^{-1} bar^{-1}, while the rejection was remained constant at 97 ± 2% as compared to that of the bare membrane (33 ± 0.48%). This implies that membrane properties including porosity, hydrophilicity, and selectivity play a key role in

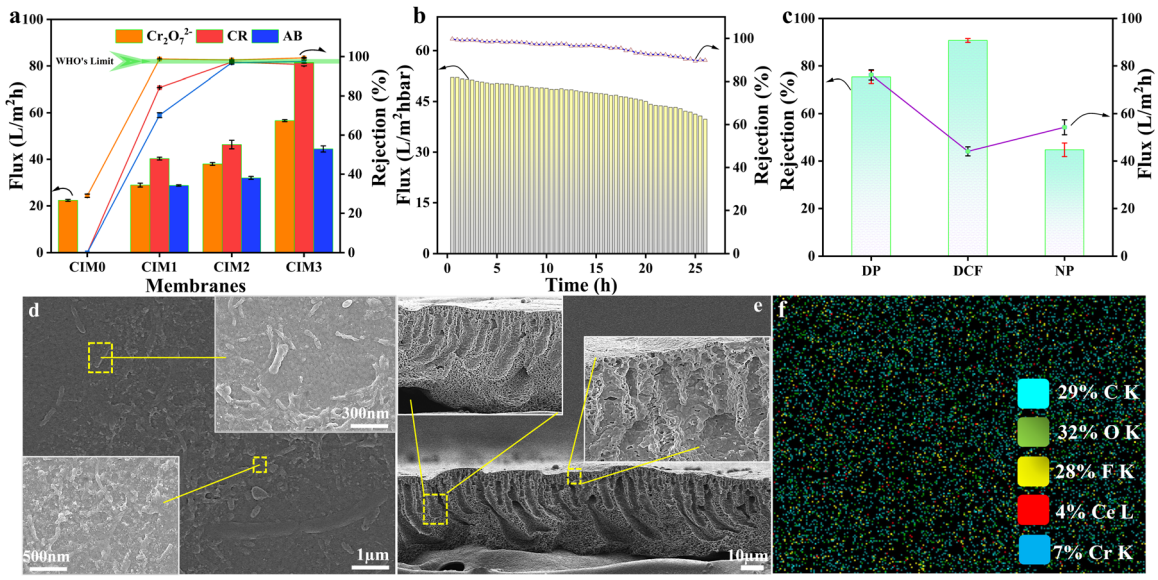

Fig. 7 (a) Flux-rejection graphs of $Cr_2O_7^{2-}$, AB & CR. (b) Long-term stability. (c) Filtration of SE (for optimized CIM_2 membrane). (d) and (e). FESEM surface and cross-sectional images of CIM_2 after long-term run (insets at a higher magnification).

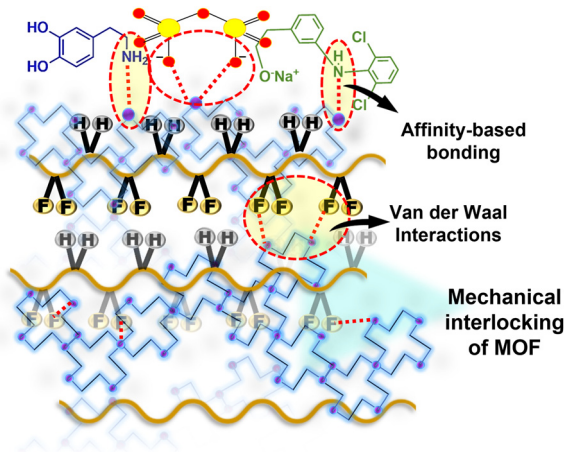

Fig. 8 Interactions involved in the removal of multi-pollutants.

rejecting $Cr_2O_7^{2-}$. CORN-MOF-2 contains carboxylate functional groups, which act as binding sites capturing chromium ions *via* strong electrostatic attractive interactions (Fig. 8). Moreover, MOF functional groups co-ordinate with chromium ions (Cr^{3+}/Cr^{6+} species such as CrO_4^{2-}), resulting in strong adsorption and rejection.[50] Since there were no carboxylate groups present in bare PVDF, no co-ordination bonding interactions were observed. Therefore, no rejection was noted.

Additionally, the performance of the fabricated membranes was extended to remove the charged dye organic pollutants AB (+) and CR (−). A feed of 25 ppm dye solution was employed and removal studies were conducted at a constant pressure of 4 bar. Fig. 7(a) shows the flux-rejection data of AB and CR. The AB flux (30.19 ± 1.04, 38.44 ± 0.32, and 43.63 ± 0.93 L m^{-2} h^{-1} bar^{-1}) and rejection (62 ± 0.54, 99 ± 0.54, and 99 ± 0.12%) both followed an increasing trend, as the MOF concentration increased from 5 to 7 wt%, which is CIM_1 < CIM_2 < CIM_3. However, no flux was collected for CIM_0. A similar trend was found for CR with the highest flux of 83.13 ± 0.84 L m^{-2} h^{-1} bar^{-1} and a rejection rate of 98 ± 1.02% for the CIM_3 membrane. The negative surface charge of the MOF membranes sets charge-based interactions with target pollutants. The rejection of the positively charged dye AB was caused by the electrostatic attraction influenced by the negatively charged membranes. Electrostatic repulsion between negatively charged membranes and the dye CR was perceived in its efficient rejection. The absence of any such interactions in the pristine PVDF membrane case can prove this point.

The highest rejection rates for different pollutants were tracked in the sequence DP ≈ $Cr_2O_7^{2-}$ ≈ AB ≈ CR > NP > DCF. The composite membranes proved noteworthy rejection competencies. Specifically pointing to the rejection of larger-size molecules, and positively (AB) and negatively (CR) charged dyes. The selective rejection of dyes, heavy metals, and pharmaceuticals through the CORN-MOF-2/PVDF membranes probably depends on a combination of size-exclusion, affinity-based bonding, and charge-based interactions. Moreover, the non-covalent interactions like π–π stacking are likely to be active between the aromatic rings of organic pollutants (AB, CR and PhACs) and itaconate linkers embedded within modified membranes.[51] Moreover, cerium, a redox-active lanthanide metal, plays a multifaceted role in pollutant removal. Ce^{4+} in the MOF network imparts strong Lewis acidity, which facilitates the coordination and adsorption of pollutants. Ce^{4+} sites provide coordination sites that bind with soft/borderline Lewis base groups. Moreover, Ce^{4+} enhances electrostatic attractions *via* π–π and hydrogen bonding *via* the linker structure. The presence of Ce also contributes to the chemical stability of the MOF under aqueous and mild acidic conditions, which adds significant implication for real-time wastewater streams. Collectively, these interactions take part in the enhanced rejection of target water contaminants and in reducing the concentrations of heavy metals such as chromium, residual dye levels, and pharmaceutical contaminants to levels well within the acceptable thresholds defined by the WHO [PhACs (DP): 75–7.5 μg L^{-1};[52] $Cr_2O_7^{2-}$: 50 μg L^{-1};[53] dyes (AB, CR): 0.1 mg L^{-1}[54]].

A long-term stability test was run for the CIM_2 membrane using $Cr_2O_7^{2-}$ as feed up to 25 h (Fig. 7(b)). An initial flux output of 52.09 L m^{-2} h^{-1} bar^{-1} with a rejection rate of 99.72% was well-maintained up to 13 h with minimal fluctuation (∼2%) in the removal efficiency and the flux gradually decreased by 7% reaching 48.21 L m^{-2} h^{-1} bar^{-1}. Further, this trend continued giving 90.80% rejection and a flux of 39.75 L m^{-2} h^{-1} bar^{-1} at the 25th hour. This inferred the stability of membrane to work for long hours with nominal loss of flux and removal efficiency owing to the collective effort of good structural integrity and mechanical stability of the membrane. FESEM and EDX mapping of the CIM_2 membrane at different magnifications after a long-term study was carried out (Fig. 7(d) and (f)). These micrographs indicate a minor uneven deposition of $Cr_2O_7^{2-}$ on the surface (Fig. 7(d) right & left insets), reducing the membrane performance; however, the cross-section of the membrane did not show any changes even in higher magnification images (Fig. 7(e) insets). This depicts the structural stability of the membrane after a long-term run. Further, the deposited $Cr_2O_7^{2-}$ was mapped on the CIM_2 surface by EDX (Fig. 7(f)). A slight difference in the elemental composition of the membrane before and after the run was noted, which indicated that the deposited pollutant possibly masked the original elemental signals, giving reduced atomic percentage of the original membrane elements.

2.3.3 Removal of PhACs from secondary effluents (SEs). This study examined the feasibility of the as-fabricated membranes by a real-time filtration study in addition to a thorough investigation of the composite membrane's filtration effectiveness. In the best scenario, SE was filtered through the CIM_2 membrane under the previously mentioned operating conditions. The wastewater used in the experiments was collected from STP Bangalore, India, accommodating 1000 equivalent citizens. In this study, 5 mg of each drug was added to the feed water to guarantee the accuracy of the applied analytical methods. The effluent characteristics are listed in Table S3. The observed flux trend differed slightly compared to the simulated samples in the order of 76.27 ± 2.10, 44.09 ± 1.90,

and 54.24 ± 3.15 L m^{-2} h^{-1} for DP, DCF, and NP, respectively (Fig. 7(c)). The rejection efficiency of PhACs varied significantly, but the observed flux rates were consistent with the case of filtering simulated samples. The reported rejection rates were 75.36 ± 2.43% for DP, 90.74 ± 1.65% for DCF, and 44.74 ± 2.11% for NP. It is important to note that, in contrast to trials using simulated samples, the CIM_2 membrane demonstrated comparatively high efficiency during the actual wastewater trials. The wastewater contained several organic species that were determined to be COD in addition to the medications. Drugs easily adsorb onto this suspended organic matter, increasing the removal effectiveness.[55] Further, investigating the different degrees of drug sorption highlighted the effective entrapment of DCF in organic and inorganic matrices over other drugs.[56] The existing organic constituents could compete with the drugs during the filtration process and result in different rejection rates. However, this notable disparity suggests that mechanisms beyond the mere adsorption and competition of other drugs are involved. The overall conclusion of this comparative study is that the as-fabricated membranes have the potential to be genuine alternatives to commercial membranes in wastewater treatment.

2.3.4 Antifouling characteristics. Following the rejection studies, fouling experiments were demonstrated by investigating the antifouling properties of composite membranes (Fig. 9(a) and (b)). Comparing the FRR, R_r, R_{ir}, and R_t values of the composite membranes to those of the parent PVDF membrane allows for a numerical explanation for the antifouling improvement (Fig. 9(b)). A low flux of 2.72 ± 0.91 L m^{-2} h^{-1} bar^{-1} before fouling and 1.09 ± 0.41 L m^{-2} h^{-1} bar^{-1} after fouling was shown by the bare PVDF membrane. Out of 37% total fouling (R_t), about 11% of fouling was reversed (R_r), and the rest 26% was irreversible fouling R_{ir}. Increased fluxes of 31.07 ± 7.98 and 28.26 ± 6.35 L m^{-2} h^{-1} bar^{-1} before fouling was shown by membranes with 5 and 7 wt% MOF concentrations. However, the flux decreased to 12.39 ± 2.65 and 20.91 ± 6.55 L m^{-2} h^{-1} bar^{-1} after fouling. A drastic decrease in flux after BSA filtration shows poor flux recovery ratios (FRRs) of 31 and 50% with about 20% reversible fouling for CIM_1 and CIM_3. With a high FRR of 96%, the CIM_2 membrane demonstrated the ability to recover a substantial amount of flux after fouling. This is an important metric since it indicates how well the membrane can function for a full twelve hours. When compared to pristine PVDF, the CIM_2 membrane exhibited a relatively high R_r value of 54% and the lowest R_{ir} value of 7%.[57,58] This indicates that the fouling that occurred could be readily reversed, most probably due to the Ce-MOF's high hydrophilicity. This feature is beneficial because it lowers the need for frequent cleaning. Overall, the results point to the potential of the MOF/PVDF membranes for antifouling characteristics over extended runs in water treatment applications.

The long-term study experimental data conducted for the optimized CIM_2 membrane reflect that the total amount of water filtered is 1.3 litres over 25 hours. The composite membrane retains more than 90% of its initial removal efficiency even after 25 h, with only a minor decline of ~7% in flux and rejection. Moreover, the highest FRR of 96% achieved during the continuous filtration of BSA for consecutive 3 cycles indicates the membrane operability for prolonged time without compromising the membrane performance. These results validate that the membrane can be reliably used for 3 cycles without regeneration. However, mild regeneration of the membrane by backwashing will restore the performance for further runs. This collectively remarks on the membrane operational longevity.

2.3.5 Comparison with the literature. This section includes a brief overview of recent literature evaluating the performance metrics of the reported composites comparing the current work (Table 2).

Membrane filtration and adsorption using specialized materials such as GO and CNTs are employed for the removal of pharmaceutically active compounds. However, these methods often target specific pharmaceutical compounds, limiting their broader applicability. Recent studies have reported efficient Cr(VI) removal using nanomaterials such as metal oxide composites and biocompatible processes. While these methods are effective, they still suffer from high operational costs and limited scalability. Dye removal studies have primarily focused on using single-adsorbent materials/membranes to target specific dyes. The studies using activated carbon, zeolites, or MOFs have shown high adsorption capacities but are limited to

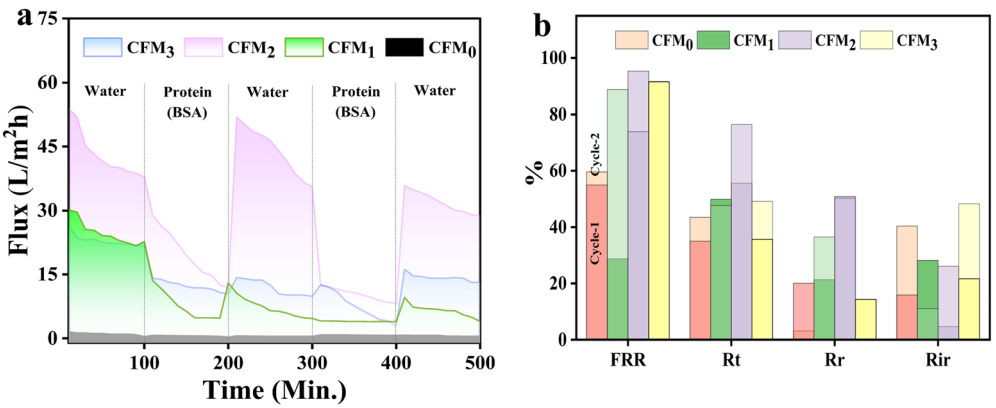

Fig. 9 (a) Flux profile of water-BSA. (b) Antifouling parameters of the PVDF membranes.

Table 2 Comparison of the current work with the recent literature

Composites	Method	Feed characteristics (concentration mg L^{-1})	Permeance ($L\ m^{-2}\ h^{-1}$)	Rejection (%)	Ref.
Polyamide/HKUST-1 BTFC membrane	Interfacial synthesis	Diclofenac (1)	33.1	99.5	59
		Naproxen (1)	24.9	98.3	
Tannic acid/chitosan/UiO-66/polyethersulfone membrane	Physical mixing and deposition	Acid brilliant scarlet (20)	18–32	99	60
		Methylene blue (20)		99	
		Cr(VI) (10)		99	
Biocompatible Zr-MOF (MIP-202)	Adsorption	Direct red 81 (5)	—	36.07 mg g^{-1}	31
		Cr(VI) (5)		19.01 mg g^{-1}	
Graphene oxide-single-wall carbon nanotube buck paper self-standing membrane	Wet method *via* vacuum filtration	Diclofenac	—	59.28	61
		Ketoprofen		58.75	
		Naproxen (1–50)		63.54	
MIL-88A/polyacrylonitrile Nanofiber membrane	Electrospinning	Amarnath red (20)	—	99.2	62
		Rhodamine B (20)		94.4	
		Acid blue (20)		99.8	
UiO-66-NH_2/TiO_2/polyethersulfone/ polyacrylonitrile nanofibers	Electrospinning	Phenol (50)	475–739	99	63
		Cr(VI) (100)		83.5	
Polyethersulfone/PMO-PPD/CQD membranes	Blending/phase inversion	Pb(II) (30)	81.3	89.76	64
		Methyl orange (40)		93.71	
		NaCl (200)		36.77	
In-MOF/PVDF membranes	Blending	Methylene blue (50)	—	99	65
		Azure A (50)		99	
		Azure B (50)		99	
		Toluidine blue O (50)		99	
CORN-MOF-2/PVDF membranes	Blending/phase inversion	Dopamine	357–443	99	This work
		Diclofenac		54	
		Naproxen		58	
		$Cr_2O_7^{2-}$		99	
		AB		99	
		CR		98	

individual dye species. Addressing the limitations of the pollutant-specific removal methods, the current study offers a comprehensive solution effective against a wide range of dyes, heavy metals, and pharmaceutical compounds. This also reduces the need for multiple, specialized treatment processes. The integration of multi-pollutant removal capabilities improves the treatment efficiency and aligns with the growing need for sustainable and adaptable water management practices in diverse industrial and municipal contexts.

Despite the CORN-MOF-2(Ce)/PVDF composite membranes acting as a single process system to remove multiple pollutants efficiently, the current approach is limited by certain tailbacks. The MOF loading beyond a certain threshold causes particle agglomeration and defects in the membrane matrix, reducing mechanical integrity. The current synthesis protocols, although effective, will not be suitable for industrial-scale production. Exploring the MOF-functionalization strategies enhances the dispersibility and compatibility. Present studies have been performed in controlled laboratory environments. Long-term studies under real wastewater conditions, including complex matrices (interfering ions), pH fluctuations, and salinity have not yet been fully validated. Accessing the collective inference of all these factors should be applied to align the current findings with industrial needs.

3. Conclusion

In this work, novel CORN-MOF-2(Ce) was synthesized employing a low-cost biocompatible organic linker-itaconic acid. The impact of infused MOF enhanced the perm-selectivity of modified membranes, transitioning the removal efficiency to the optimal 99% for DP, $Cr_2O_7^{2-}$ and AB and CR with flux rates of 101 ± 13, 36 ± 2, 26 ± 1.5, and 45 ± 4 L m^{-2} h_{-1} and 54 and 58% for NP and DCF with flux rates of 78 ± 3 and 59 ± 2 L m^{-2} h^{-1}, respectively. The removal rates of PhACs were further substantiated in different pH ranges, attaining a peak performance at neutral pH values. The real-time monitoring of PhACs in the secondary effluent (SE) has revealed the efficiency of the optimized 7 wt% membrane with superior rejection rates in the order of DCF > DP > NP (90.7 > 75.3 > 44.7%, respectively). The highlighted antifouling characteristic of the membranes recovered 96% flux (FRR) after 3 cycle fouling tests. Overall, this work highlights a transformative approach to wastewater treatment through the simultaneous removal of the dyes AB and CR, the heavy metal $Cr_2O_7^{2-}$, and the pharmaceutical actives DP, DCF, and NP. This multi-pollutant removal strategy addresses the limitations of conventional methods that target individual contaminants, offering a comprehensive, efficient, and environmentally sustainable solution. By integrating diverse removal mechanisms into a single system, our method ensures high treatment efficiency across complex and different wastewater compositions. These membranes pave the way for scalable and cost-effective applications in industrial and municipal wastewater management, contributing to cleaner water resources. The ability of the membrane developed in this research study to consistently meet the WHO standards highlights its effectiveness and reliability as a sustainable solution for addressing water pollution challenges.

Author contributions

Usha Nellur: conceptualization, methodology, software, validation, formal analysis, investigation, data curation, visualization, writing – original draft. Mahesh Padaki: supervision, project administration, funding acquisition, writing – review & editing.

Conflicts of interest

The authors declare no conflict of interest.

Data availability

The data supporting this article have been included as part of the SI. Supplementary information: Additional characterization and experimental results. See DOI: **https://doi.org/10.1039/d5ma00581g**

References

1 V. S. Silveira, A. S. de Vargas, É. Hansen, L. C. Robinson, N. A. Thoen, D. M. de Quevedo, E. L. Schneider and P. M. de Aquim, *Waste and Biomass Valorization*, 2023, **14**, 377–387.
2 P. Xie, Z. Liu, J. Li, D. Ju, X. Ding, Y. Wang and J. C. Hower, *Chemosphere*, 2023, **317**, 137908.
3 A. Bhardwaj, S. Kumar and D. Singh, *Water Qual. Res. J.*, 2023, **58**, 128–152.
4 **https://Www.Dyes-Pigment.Com/Leather-Dyes.Html#:~:Text=If%20we%20see%20from%20the,70%25%20of%20all%20leather%20dyeing**.
5 S. M. Zainab, M. Junaid, N. Xu and R. N. Malik, *Water Res.*, 2020, **187**, 116455.
6 S. Kumari, A. Sharma, P. Dhiman, M. Thakur, Z. Aloui, M. Selvaraj and A. Kumar, *Mater. Sci. Eng. B*, 2025, **314**, 118009.
7 A. Kumari, A. Kumar, D. Pathania, M. Thakur and A. Sharma, *Sustain. Chem. Environ.*, 2025, **9**, 100189.
8 S. Devi, P. Dhiman, A. Sharma, S. Gautam and A. Kumar, *Next Mater.*, 2025, **7**, 100348.
9 F. Zheng and Y. Wang, *J. Membr. Sci.*, 2022, **659**, 120836.
10 Z. Wang, I. Pacheco-Fernández, J. E. Carpenter, T. Aoyama, G. Huang, A. Pournaghshband Isfahani, B. Ghalei, E. Sivaniah, K. Urayama, Y. J. Colón and S. Furukawa, *Commun. Mater.*, 2024, **5**, 161.
11 X.-J. Hu, Y.-L. Li, H.-X. Liu, S.-M. Ying, Q. Yin and T.-F. Liu, *RSC Adv.*, 2024, **14**, 12142–12146.
12 S.-Y. Fang, J.-L. Gong, L. Tang, J. Li, M. Qin, H.-Y. Zhou, L.-X. Tang and J. Zhao, *ACS Appl. Mater. Interfaces*, 2023, **15**, 25633–25649.
13 U. Nellur, P. S. Goh, M. Padaki and A. F. Ismail, *J. Mater. Chem. C*, 2025, **13**, 12087–12097.
14 T. Klement and J. Büchs, *Bioresour. Technol.*, 2013, **135**, 422–431.
15 T. Cordes, A. Michelucci and K. Hiller, *Annu. Rev. Nutr.*, 2015, **35**, 451–473.
16 F. E. Chen, R. M. Mandel, J. J. Woods, J. H. Lee, J. Kim, J. H. Hsu, J. J. Fuentes-Rivera, J. J. Wilson and P. J. Milner, *Chem. Sci.*, 2021, **12**, 7848–7857.
17 J. Hu, W. Deng and D. Chen, *ACS Sustainable Chem. Eng.*, 2017, **5**, 3570–3582.
18 R. Xu, Q. Ji, P. Zhao, M. Jian, C. Xiang, C. Hu, G. Zhang, C. Tang, R. Liu, X. Zhang and J. Qu, *J. Mater. Chem. A*, 2020, **8**, 7870–7879.
19 A. S. Chevinly, H. G. Mobtaker, T. Yousefi, A. S. Shirani and H. Aghayan, *Inorg. Chim. Acta*, 2017, **455**, 34–40.
20 X. Mi and X. Li, *Sep. Purif. Technol.*, 2022, **301**, 122006.
21 X. Han, Z. Liu, M. F. Bakhtari, J. Luo and L. Deng, *Environ. Eng. Res.*, 2023, **28**, 220647.
22 A. H. Wibowo, Y. I. F. Hasanah, M. Firdaus, D. M. Widjonarko and J. Cepeda, *J. Environ. Chem. Eng.*, 2018, **6**, 2910–2917.
23 D. M. Patil, G. A. Phalak and S. T. Mhaske, *Des. Monomers Polym.*, 2017, **20**, 269–282.
24 M. Damilola Olawale, J. Obaleye, M. D. Olawale, J. A. Obaleye and E. O. Oladele, *Niger. Res. J. Chem. Sci.*, 2020, **8**, 2020.
25 C. Zhu, T. Ding, W. Gao, K. Ma, Y. Tian and X. Li, *Int. J. Hydrogen Energy*, 2017, **42**, 17457–17465.
26 Y. Zhang, X. Zeng, X. Jiang, H. Chen and Z. Long, *Microchem. J.*, 2019, **149**, 103967.
27 S. A. Mntambo, P. S. Mdluli, M. M. Mahlambi, S. C. Onwubu and N. L. Nxumalo, *Water SA*, 2019, **45**, 131–140.
28 T. Wu, B. Zhou, T. Zhu, J. Shi, Z. Xu, C. Hu and J. Wang, *RSC Adv.*, 2015, **5**, 7880–7889.
29 I. Y. Abdullah, M. H. H. Jumali, M. Yahaya and H. M. Shanshool, *Adv. Environ. Biol.*, 2015, **9**, 20–27.
30 X. Chen, B. Zhao, P. Han, W. Fu and L. Chen, *React. Funct. Polym.*, 2014, **84**, 10–20.
31 K. E. Diab, E. Salama, H. S. Hassan, A. Abd El-moneim and M. F. Elkady, *Sci. Rep.*, 2021, **11**, 1–13.
32 Y. Sui, Z. Wang and C. Gao, *Desalin. Water Treat.*, 2014, **52**, 6377–6388.
33 G. Yi, J. Li, L. C. Henderson, W. Lei, L. Du and S. Zhao, *Polymers*, 2022, **14**(21), 4599.
34 S. Acarer Arat, İ. Pir, M. Tüfekci, N. Öz and N. Tüfekci, *Polymers*, 2024, **16**, 3531.
35 S. Song, Z. Zheng, Y. Bi, X. Lv and S. Sun, *J. Mater. Sci.*, 2019, **54**, 3832–3846.
36 U. ur R. Farooqui, A. L. Ahmad and N. A. Hameed, *J. Phys. Sci.*, 2018, **29**, 125–132.
37 U. Nellur, N. S. Naik, R. M. Rego, M. Kigga, G. Arthanareeswaran and M. Padaki, *Environ. Sci.: Water Res. Technol.*, 2023, **9**, 1216–1230.
38 U. Nellur, K. K S, N. S. Naik and M. Padaki, *J. Cleaner Prod.*, 2024, **483**, 144268.
39 I. M. Bernhardsen, L. Ansaloni, H. K. Betten, L. Deng and H. K. Knuutila, *Sep. Purif. Technol.*, 2019, **222**, 188–201.
40 K. Umam, F. Sagita, E. Pramono, M. Ledyastuti, G. T. M. Kadja and C. L. Radiman, *JCIS Open*, 2023, **11**, 100093.
41 H. Bai, X. Wang, Y. Zhou and L. Zhang, *Prog. Nat. Sci. Mater. Int.*, 2012, **22**, 250–257.

42 B. J. Ryan and K. M. Poduska, *Am. J. Phys.*, 2008, **76**, 1074–1077.
43 X. Chen, Y. He, Y. Fan, G. Zeng and L. Zhang, *Sep. Purif. Technol.*, 2019, **212**, 326–336.
44 N. Zhang, N. Yang, L. Zhang, B. Jiang, Y. Sun, J. Ma, K. Cheng and F. Peng, *Chem. Eng. J.*, 2020, **402**, 126200.
45 G. Feng, H. Zhang, J. Chen, Z. Fang and X. Hu, *J. Environ. Chem. Eng.*, 2025, **13**, 115172.
46 F. Ke, C. Peng, T. Zhang, M. Zhang, C. Zhou, H. Cai, J. Zhu and X. Wan, *Sci. Rep.*, 2018, **8**, 1–11.
47 N. A. Shafie, M. N. Abu Seman, S. M. Saufi and A. W. Mohammad, *Chem. Eng. Res. Des.*, 2023, **200**, 186–201.
48 Z. Hasan, J. Jeon and S. H. Jhung, *J. Hazard. Mater.*, 2012, **209–210**, 151–157.
49 Z. Hasan, E. Choi and S. H. Jhung, *Chem. Eng. J.*, 2013, **219**, 537–544.
50 B. T. I. Ali, H. S. A. Bay, H. Saputra, S. Pati Senda and N. Widiastuti, *Chem. Eng. J.*, 2024, **493**, 152667.
51 T. AlAbdulaal, M. A. Assiri, M. I. Mohammed, H. Y. Zahran, F. A. Harraz, M. S. Al-Assiri, I. S. Yahia and M. A. Ibrahim, *Opt. Quantum Electron.*, 2022, **54**, 778.
52 I. Alessandretti, C. V. T. Rigueto, M. T. Nazari, M. Rosseto and A. Dettmer, *J. Environ. Chem. Eng.*, 2021, **9**, 106743.
53 No Title, (**https://www.barc.gov.in/technologies/dkit/index.html#:~:text=Overview,VI**) in natural water bodies.
54 R. Al-Tohamy, S. S. Ali, F. Li, K. M. Okasha, Y. A.-G. Mahmoud, T. Elsamahy, H. Jiao, Y. Fu and J. Sun, *Ecotoxicol. Environ. Saf.*, 2022, **231**, 113160.
55 J. S. Ra, S. Y. Oh, B. C. Lee and S. D. Kim, *Environ. Int.*, 2008, **34**, 184–192.
56 B. Chefetz, T. Mualem and J. Ben-Ari, *Chemosphere*, 2008, **73**, 1335–1343.
57 J. Zhao, Y. Yang, C. Li and L. Hou, *Sep. Purif. Technol.*, 2019, **209**, 482–490.
58 Z. Zhou, L. Xu, X. Zhu, Q. Wang, X. Meng and T. Huhe, *Chemosphere*, 2023, **337**, 139317.
59 L. Paseta, D. Antorán, J. Coronas and C. Téllez, *Ind. Eng. Chem. Res.*, 2019, **58**, 4222–4230.
60 P. Shi, X. Hu and M. Duan, *J. Cleaner Prod.*, 2021, **290**, 125794.
61 M. Baratta, A. Tursi, M. Curcio, G. Cirillo, A. V. Nezhdanov, A. I. Mashin, F. P. Nicoletta and G. De Filpo, *Molecules*, 2022, **27**(22), 7674.
62 H. Wu, L. Xu, J. Jia, F. Dong, Y. Jia and X. Liu, *Molecules*, 2023, **28**, 760.
63 S. Koushkbaghi, H. A. Kermani, S. Jamshidifard, H. Faramarzi, M. Khosravi, P. G. Abadi, F. S. Jazi and M. Irani, *RSC Adv.*, 2023, **13**, 12731–12741.
64 F. Mehrjo and A. Shahbazi, *Environ. Sci.: Water Res. Technol.*, 2025, **11**(2), 435–448.
65 K. Maru, S. Kalla and R. Jangir, *Langmuir*, 2024, **40**, 8144–8161.